ARTICLE

Formation of the Mantoverde iron oxide-copper-gold (IOCG) deposit, Chile: insights from Fe and O stable isotopes and comparisons with iron oxide-apatite (IOA) deposits

Tristan M. Childress[1] · Adam C. Simon[1] · Martin Reich[2] · Fernando Barra[2] · Mauricio Arce[3] · Craig C. Lundstrom[4] · Ilya N. Bindeman[5]

Abstract

The Mantoverde iron oxide-copper-gold (IOCG) deposit, Chile, contains hundreds of millions of tonnes (Mt) of mineable iron oxide and copper sulfide ore. While there is an agreement that mineralization at Mantoverde was caused by hydrothermal fluid(s), there is a lack of consensus for the role(s) that non-magmatic vs. magmatic fluid(s) played during the evolution of the mineralized system. In order to overcome the hydrothermal overprint at Mantoverde, which is known to disturb most conventional stable isotope systems (e.g., oxygen), we report the first $\delta^{56}Fe$ and $\delta^{18}O$ pairs for early-stage magnetite and late-stage hematite that provide information on the source reservoir of the hydrothermal fluids. Magnetite $\delta^{56}Fe$ values range from 0.46 ± 0.04 to $0.58 \pm 0.02‰$ and average $0.51 \pm 0.16‰$ ($n = 10$; 2σ). Three hematite $\delta^{56}Fe$ values were measured to be 0.34 ± 0.10, 0.42 ± 0.09, and 0.46 ± 0.06. Magnetite $\delta^{18}O$ values range from 0.69 ± 0.04 to $4.61 \pm 0.05‰$ and average $2.99 \pm 2.70‰$ ($n = 9$; 2σ). Hematite $\delta^{18}O$ values range from -1.36 ± 0.05 to $5.57 \pm 0.05‰$ and average $0.10 \pm 5.38‰$ ($n = 6$; 2σ). These new $\delta^{56}Fe$ and $\delta^{18}O$ values fingerprint a magmatic-hydrothermal fluid as the predominant ore-forming fluid responsible for mineralization in the Mantoverde system.

Keywords Kiruna · Chilean Iron Belt · Magnetite · Hematite · Iron oxide-copper-gold · IOCG · Iron oxide-apatite · IOA

Introduction

Iron oxide-copper-gold (IOCG) deposits contain variable quantities of their namesake metals, and some deposits contain mineable grades of rare earth elements (REE), P, U, Ag, Co, Ba, and F (Sillitoe 2003; Williams et al. 2005; Groves et al. 2010; Barton 2014). Since the discovery in the 1970s of the giant Precambrian Olympic Dam deposit in Australia, investigations of IOCG deposits have focused on determining the source reservoir(s) hydrothermal fluids in order to develop a genetic model that explains mineralization and can be used to guide exploration strategies (Roberts and Hudson 1983;

Editorial handling: M. Fayek

✉ Tristan M. Childress
   tristanc@umich.edu

   Adam C. Simon
   simonac@umich.edu

   Martin Reich
   mreich@cec.uchile.cl

   Fernando Barra
   fbarrapantoja@ing.uchile.cl

   Mauricio Arce
   mauricio.arce@mantoscopper.com

   Craig C. Lundstrom
   lundstro@illinois.edu

   Ilya N. Bindeman
   bindeman@uoregon.edu

Extended author information available on the last page of the article

Hitzman et al. 1992; Porter 2000; Williams et al. 2005; Groves et al. 2010; Mumin et al. 2010; Richards and Mumin 2013a, b; Barton 2014; Simon et al. 2018). Working hypotheses to explain the origin of the ore-forming fluid and genesis of include: (1) magmatic-hydrothermal fluid (e.g., Pollard 2006; Nyström et al. 2008; Rieger et al. 2010, 2012; Jonsson et al. 2013; Knipping et al. 2015a, b; Reich et al. 2016); (2) non-magmatic-hydrothermal fluid(s) such as meteoric or basinal fluids driven by heat from either a magma body or the crustal geotherm (e.g., Barton and Johnson 1996; Sillitoe and Burrows 2002; Benavides et al. 2007); (3) metamorphic hydrothermal fluids derived from metamorphic devolatilization and water-rock interaction (Fisher and Kendrick 2008); and (4) magmatic-hydrothermal fluid evolved from a volatile-bearing iron oxide melt, which itself evolved via liquid immiscibility from a silicate magma (Nyström and Henríquez 1994; Travisany et al. 1995; Naslund et al. 2002; Tornos et al. 2016).

The lack of consensus for any genetic model stems from (1) a lack of correlation between IOCG deposits and specific tectonic or magmatic settings and (2) a lack of geochemical constraints on the source of the hydrothermal fluids. Adding to the controversy is the recognized spatial and temporal association of IOCG and iron oxide-apatite (IOA) deposits that led Sillitoe (2003) to propose that IOCG systems transition at depth to IOA mineralization. If IOCG and IOA deposits do represent parts of a single evolving ore system, then any viable genetic model that explains one must explain the other. Studies at the world class Los Colorados IOA deposit, Chile, support the hypothesis for a genetic connection between IOCG and IOA deposits (Knipping et al. 2015a, b; Bilenker et al. 2016; Reich et al. 2016; Barra et al. 2017; Deditius et al. 2018; Simon et al. 2018), consistent with IOCG mineralization resulting from a magmatic-hydrothermal fluid, which contains sufficient dissolved metals and S after IOA ore formation to form IOCG mineralization at shallower levels of the crust. These studies do not eliminate the potential importance of non-magmatic fluids, which may mix with ascending S- and metal-enriched magmatic-hydrothermal fluids and promote mineralization. However, the degree of influence of non-magmatic fluid(s) on ore formation remains controversial, and the primary source reservoir of ore metals remains unconstrained in most IOCG deposits.

In this study, we focus on samples collected from one drill core between the Laura and Mantoverde Norte ore bodies in the world-class Mantoverde IOCG system in the Chilean Iron Belt (Fig. 1). New stable Fe and O isotope data are reported for magnetite and hematite that fingerprint a magmatic source reservoir for these modally dominant constituents in the orebodies. We also present stable Fe and O isotope data from IOA deposits in the Chilean Iron Belt and other mineralized districts and use the combined data set to discuss the evolution of Mantoverde as

part of a continuum where S–Cu–Au-poor iron oxide-apatite mineralization represents the deeper levels of systems that transition from IOA mineralization at depth to IOCG mineralization at shallow levels of the crust.

Geologic background

The Mantoverde deposit is located approximately 50 km east of the Pacific coastline in northern Chile within the Atacama Fault Zone (AFZ) system in the Chilean Iron Belt. The formation of the Chilean Iron Belt is associated with the subduction of the Aluk plate beneath South America that led to arc and associated back-arc basin formation during Jurassic–Early Cretaceous magmatism, which developed on Late-Paleozoic to Triassic basement (Mpodozis and Ramos 1990). Late Jurassic andesitic volcaniclastic conglomerates, breccias, or flows make up the majority of rock types within the Chilean Iron Belt. These volcanic rocks were subsequently intruded by Cretaceous granitoids of the Chilean Coastal Batholith (Lara and Godoy 1998), including subalkaline to alkaline, metaluminous, magnetite series, I-type granitoids of the calc-alkaline suite ranging from diorite to granodiorite, tonalite, and monzodiorite to quartz monzodiorite, all of which range in age from 90 to 130 Ma (Rieger et al. 2010; Barra et al. 2017). The majority of volcanic rocks within the Mantoverde IOCG district belong to the Late Jurassic La Negra Formation and Early Cretaceous Punta del Cobre Formation (Benavides et al. 2007). The Mantoverde IOCG deposits themselves are hosted in basaltic andesite and andesite flows and volcaniclastic rocks correlated with the La Negra Formation (Lara and Godoy 1998). The regionally extensional, north-south trending strike-slip Atacama Fault Zone transects both the arc and basement rocks, and the region is covered by Neogene to Quaternary alluvial and colluvial deposits.

The central and eastern branches of the Atacama Fault Zone in the Mantoverde district mark the western and eastern limits of IOCG mineralization in the Mantoverde system and are connected by the NW-trending, east-dipping Mantoverde Fault, which is interpreted to be a scissor fault (Fig. 1; Zamora and Castillo 2001; Rieger et al. 2012). The Mantoverde Fault is considered to be the main hydrothermal fluid conduit and hosts the majority of mineralization in the deposit. Mineralization resulted from three major fluid events that define the paragenetic stages as described by Rieger et al. (2010): (1) the early iron oxide stage, (2) the sulfide stage, and (3) the late stage. Benavides et al. (2007) reported slightly different paragenetic relations and separated them into stages I, II, III, and IV, where stage I is responsible for magnetite mineralization, stage II is responsible for hydrolytic alteration resulting in minor hematite and pyrite,

Fig. 1 Map of the Mantoverde
district showing general geology,
structures, iron oxide deposits,
and the location of the drill hole
from which samples were
collected. The inset shows the
location of the deposit (source:
Rieger et al. 2012)
AA
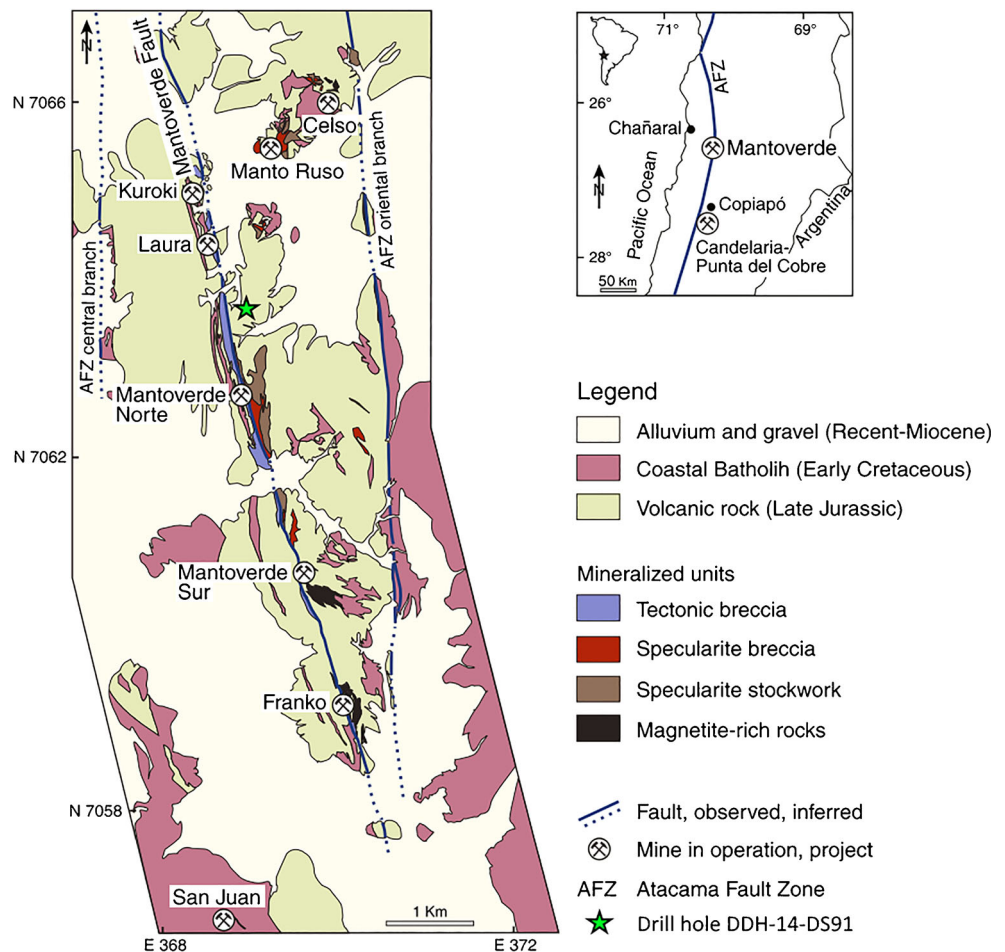
stage III is responsible for the majority of hematite miner-
alization, and stage IV resulted in terminal calcite and quartz
veining. We follow the paragenetic scheme of Rieger et al.
(2010). The deposit is zoned with magnetite dominating at
depth and hematite at shallow or distal levels of the
Mantoverde Fault. The oxidation level reaches between
200 and 250 m below the surface and marks the transition
of the supergene zone to the hypogene zone where pyrite
and chalcopyrite are commonly present (Rieger et al. 2012).
Mineralization styles adapted from Vila et al. (1996) and
Rieger et al. (2010) are summarized in Table 1.

Methods

Sample selection and preparation

Magnetite and hematite were sampled from a single drill core
DDH-14-DS91, over a depth of depth of 262 to 492 m, located
between the Mantoverde Norte and Laura ore bodies (Fig. 1).
Several fragments of rock from each sampled depth and thin
sections of samples from five depths (291, 340, 355, 456, and
492 m) were prepared for optical characterization and electron

probe microanalysis. For isotope analyses, magnetite grains
were sampled where present, and hematite from veinlets was
sampled where magnetite was not present. Iron oxides are not
abundantly present at all depths and consequently were not
sampled at every depth. The collected samples are represen-
tative of multiple mineralization styles in the Mantoverde sys-
tem (ESM Table 1).

Sample descriptions

Massive magnetite is the modally dominant mineral in the
upper parts of the core, from 262 to 314 m, and becomes
more disseminated with depth. Potassium feldspar and
chlorite are the dominant matrix-forming minerals
throughout the core, with common but varying amounts
of sericite after K-feldspar. Pyrite is a major mineral in the
upper parts of the core (262 to 314 m) where it occurs as
large blotches and filling veins. Chalcopyrite is a modally
minor (< 5 vol.%) mineral and occurs with greater abun-
dance than pyrite in the K-feldspar-rich samples at depth.
Specularite veinlets (≤ 1–2 mm), K-feldspar veinlets (0.5–
1.5 mm), and calcite veinlets (0.2–5 mm) occur pervasive-
ly throughout the drill core, and quartz occurs as a minor

Table 1 Major characteristics of deposits

Deposit	General	Major mineralization
Manto Ruso	Large ore zone with both supergene and hypogene copper ore; east of Mantoverde fault; contains primarily hematite with local magnetite-rich rocks	Specularite-cemented hydrothermal breccia with andesite and diorite fragments affected by strong K-feldspar alteration and silicification ± chloritization. Pyrite, chalcopyrite, and, locally, bornite and digenite occur interstitial to specularite; breccia grades to specularite stockwork zone containing chalcopyrite-pyrite; host rocks characterized by strong pervasive quartz, K-feldspar, or sericite alteration ± chlorite alteration.
Mantoverde Norte	Hosted within and proximal to the Mantoverde fault; main ore-bearing units all parallel the fault; contains supergene copper oxides	Specularite-calcite hydrothermal breccia with andesite or granitoid clasts commonly affected by variable K-feldspar alteration with chloritization, sericitization, silicification, and/or carbonatization; cut by K-feldspar ± quartz, tourmaline, sericite, calcite, and specularite veinlets pyrite, chalcopyrite, digenite present
Mantoverde Sur	Weak relation to Mantoverde fault; magnetite stockworks and disseminations; pervasive argillic alteration	Magnetite-chlorite-sericite-K-feldspar-cemented breccias, igneous clasts altered mainly by magnetite, K-feldspar, and quartz, cut by K-feldspar ± quartz, calcite, sericite, and late specularite-calcite veinlets; magnetite, mushketovite, pyrite, and chalcopyrite present

mineral in some K-feldspar veinlets. K-feldspar is more pervasive in samples at depths ≥ 331.7 m, with the K-feldspar matrix containing large blotches of microcline and thin specularite (< 0.5 mm), pyrite (~ 1 mm), and chalcopyrite (~ 1 mm) veinlets.

Magnetite analyzed in this study did not form by mushketovization of specularite, consistent with magnetite from stage I described by Benavides et al. (2007) and the paragenetic "mt II" from the iron oxide stage as described by Rieger et al. (2010). Hematite is interpreted to be that of stage III mineralization described by Benavides et al. (2007) and Late Stage mineralization by Rieger et al. (2010) due to its occurrence as veinlets and matrix-enclosing angular to subangular fragments of K-feldspathized and chloritized host rock. The magnetite and hematite grains in the size fraction used for analyses were free of weathering features and contain minimal inclusions. Figure 2 contains photos of representative samples.

EPMA and FE-SEM

An electron probe microanalyzer (EPMA) and field emission scanning electron microscope (FE-SEM) at the University of Michigan were used to acquire BSE images and to characterize the concentrations of Mg, Al, Si, Ca, Ti, V, Cr, and Mn in magnetite and hematite from the same aliquots as those processed for Fe and O stable isotope analyses. The

instrumental conditions were identical to those used in Knipping et al. (2015a, b) and are reported in Table 2 (ESM). Care was taken to analyze only magnetite and hematite that appeared texturally homogeneous under BSE examination.

Iron isotopes

Samples were prepared for isotope analyses following the methods described in Bilenker et al. (2016) and Childress et al. (2016). Magnetite and hematite samples were subjected to ion exchange chromatography to isolate Fe for isotopic analysis. Between ~ 0.3 and 0.7 mg of each sample was dissolved and dried down in aqua regia, again in 8 N HCl, and then loaded into columns of AG1-X8 resin in 8 N HCl, following the procedure described by Huang et al. (2011). Analyses were performed at the University of Illinois, Urbana-Champaign, over two sessions using a Nu Plasma HR multi-collector-inductively coupled plasma-mass spectrometer (MC-ICP-MS) in dry plasma mode with either a DSN-100 or an Aridus II Desolvating Nebulizer System. All analyses were conducted following the double-spike method of Millet et al. (2012) to correct for instrumental mass bias and increase precision. Each sample was analyzed two times, with all analyses bracketed by the international standard IRMM-14 to correct for small changes in mass bias with time (Millet et al. 2012). Iron isotope values (ESM Table 3) are reported relative to IRMM-14, calculated by using Eq. (1):
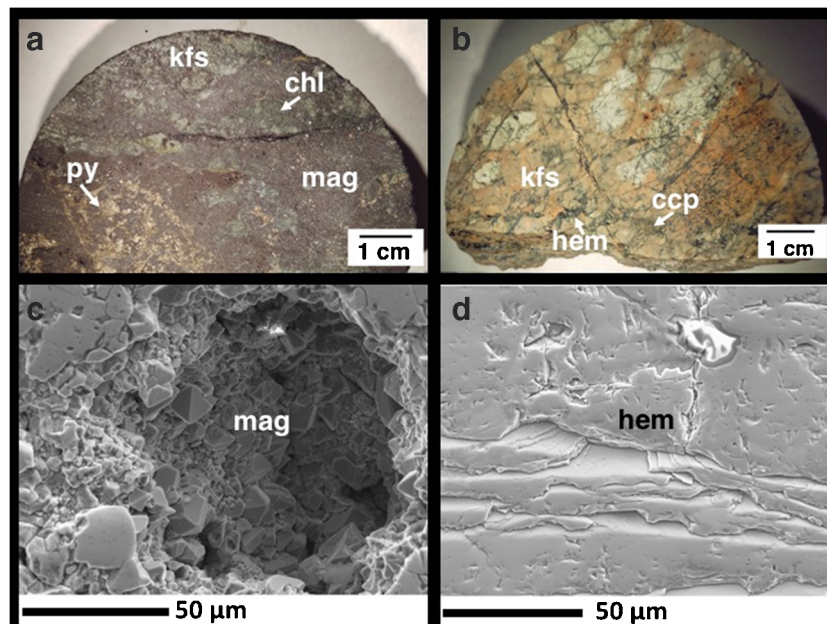
Fig. 2 Photographs of samples from drill core DDH-14-DS91 collected from depths of **a** 262 and **b** 324 m. These samples are representative of the range of textural and mineralogical composition throughout the drill core. The BSE images are representative of magnetite (**a**) and hematite (**b**) sampled for O and Fe isotope analysis and trace element EPMA from the samples shown in (**a**) and (**b**). The BSE image in (**a**) shows a cavity in massive magnetite filled with magnetite octahedra. The BSE image in (**b**) shows cleavage planes in hematite (var. specularite). The bright areas in each BSE image are the result of surface charging. Mag, magnetite; kfs, K-feldspar; py, pyrite; hem, hematite; ccp, chalcopyrite; chl, chlorite

$$\delta^{56}Fe_{sample}\ (‰)$$
$$= \left[\left(^{56}Fe/^{54}Fe\right)_{measured} / \left(^{56}Fe/^{54}Fe\right)_{IRMM-14} - 1\right] *1000\ (1)$$

The in-house standard UIFe yielded an average $\delta^{56}Fe$ value of $0.67 \pm 0.05‰$ ($n = 8$, 2σ, one session over 4 days) in the first session using the DSN-100. The international standard BCR-2 yielded a $\delta^{56}Fe$ value of $0.08 \pm 0.05‰$ ($n = 1$, 2σ; recommended value $0.091 \pm 0.011‰$; Craddock and Dauphas 2011) during the same session. The in-house standard UIFe yielded an average $\delta56Fe$ value of $0.65 \pm 0.05‰$ ($n = 2$, 2σ, one session in 1 day) using the Aridus II; BCR-2 was not measured during this session.

Oxygen isotopes

Oxygen isotope analyses of magnetite and hematite were conducted at the University of Oregon using a laser fluorination line coupled with a Thermo-Finnigan MAT 253 gas isotope ratio mass spectrometer in dual inlet mode following the methods described in Bilenker et al. (2016) and Childress et al. (2016). Magnetite and hematite grains (2–3 mg) from each sample were initially subjected to low-power lasing. Laser power was slowly increased to minimize jumping movements of the grains during fluorination with BrF_5. For samples that did not experience grain jumping, O_2 yields were close to the theoretical 100%. All data were compared with the Gore Mountain garnet (GMG) standard, which was measured before, during, and after analysis of magnetite samples. Oxygen isotope values (ESM Table 4) are reported relative

Table 2 O and Fe stable isotope ratios of magnetite and hematite

Sample	δ18O (‰)	2σ	μmol/g	δ56Fe (‰)	2σ
262mmt	1.57	0.09	8.5	0.54	0.05
276mmt	0.69	0.03	7.9	0.55	0.02
284mmt	4.01	0.05	6.8		
291mmt	4.58	0.06	10.4		
298mmt	2.34	0.06	8.5	0.61	0.04
305mmt	3.62	0.07	8.6	0.50	0.04
314mmt	2.50	0.08	8.9	0.58	0.02
331mmt				0.37	0.06
340mmt	4.61	0.11	6.0	0.46	0.04
411mmt	3.02	0.06	4.9	0.53	0.04
438mmt				0.55	0.06
471mmt				0.38	0.02
276m hmt	− 1.16	0.2*	8.0		
314m hmt	− 0.67	0.2*	8.6		
449m hmt	− 1.36	0.09	5.8	0.34	0.10
455m hmt	− 0.96	0.04	9.2	0.42	0.09
489m hmt	− 0.84	0.08	9.1	0.46	0.06
492m hmt	5.57	0.11	9.3		

Theoretical yields for magnetite are 7.8 and 10.4 μmol/g. Blank spaces indicate samples that were not analyzed for either Fe or O

to the international Vienna Standard Mean Ocean Water (VSMOW). Average values for standard GMG ($\delta^{18}O_{GMG} \pm 1\sigma$) over 3 days of measurements were 7.23 ± 0.10, 7.21 ± 0.11, and 7.19 ± 0.08‰. Analytical precision for individual analyses is ± 0.10‰. The analytical values were adjusted by the difference between our measured standard values for each day and the recommended $\delta^{18}O$ value for the GMG standard 6.52‰. Theoretical O_2 yields for magnetite and hematite are 7.8 and 10.4 μmol/g and analyzed magnetite and hematite samples average 7.8 and 8.3 μmol/g, respectively.

Results

Major and trace element concentrations of magnetite and hematite

The average concentrations of Mg, Al, Si, Ca, Ti, V, Cr, Mn, and Fe in magnetite and hematite are reported in Table 5 (ESM), and the entire EPMA data set is provided in Table 6 (ESM). The average concentrations of Fe in magnetite ($n = 335$) and hematite ($n = 195$) across all samples at all depths are 70.8 ± 1.0 and 68.8 ± 1.1 wt.%, respectively. Magnetite across all depths contains low and similar concentrations of Mg, Al, Ca, V, Cr, and Mn (average of 0.03, 0.11, 0.08, 0.07, 0.01, and 0.01 wt.%, respectively), elevated Si (0.24 wt.%), and low Ti (0.05 wt.%) relative to hematite. Hematite across all depths contains low and similar concentrations of Mg, Al, Ca, V, Cr, and Mn (0.02, 0.11, 0.05, 0.06, 0.01, and 0.01 wt.%, respectively), is depleted in Si (0.03 wt.%), and is elevated in Ti (0.56 wt.%) relative to magnetite. In general, the average trace element composition of hematite in this study is more comparable with Fe oxides from porphyry and igneous environments as reported by Dupuis and Beaudoin (2011). Variability of trace element concentrations corresponds to textural variability identified in BSE images. Some magnetite grains display oscillatory (Fig. 3a, b) and mottled zoning of trace-element-rich (dark gray; Fig. 3a–c) and trace-element-poor (light gray in Fig. 3a–c) magnetite, and some magnetite grains are concentrically zoned with a trace-element rich core surrounded by a trace-element poor rim (Fig. 3c, e, f).

Iron isotope compositions of magnetite and hematite

Stable Fe isotope ratios for magnetite and hematite are reported as $\delta^{56}Fe$ in Table 3 (ESM) and Fig. 4. The $\delta^{56}Fe$ values (± 2 sigma) for magnetite range from 0.46 ± 0.04 to 0.58 ± 0.02‰ and average 0.51 ± 0.16‰ ($n = 10$). The $\delta^{56}Fe$ values (± 2 sigma) for three late-stage hematite are 0.34 ± 0.10, 0.42 ± 0.09, and 0.46 ± 0.06‰.

Oxygen isotope compositions of magnetite and hematite

Stable O isotope ratios for magnetite and hematite are reported as $\delta^{18}O$ in Table 4 (ESM) and Fig. 5. The $\delta^{18}O$ values (± 2 sigma) for magnetite range from 0.69 ± 0.04 to 4.61 ± 0.05‰ and average 2.99 ± 2.70‰ ($n = 9$) and for late-stage hematite range from -1.36 ± 0.05 to 5.57 ± 0.05‰ and average 0.10 ± 5.38‰ ($n = 6$).

Discussion

The source of Fe and O in the Mantoverde system

Iron isotopes The $\delta^{56}Fe$ values reported here for magnetite from Mantoverde are plotted in Fig. 4 along with the globally accepted range of $\delta^{56}Fe$ for magnetite that grows from silicate melt and magmatic-hydrothermal fluid, and non-magmatic low-temperature hydrothermal fluid (Heimann et al. 2008; Bilenker et al. 2016; Childress et al. 2016; Troll et al. 2019). The $\delta^{56}Fe$ data for Mantoverde are within the published range for magmatic and magmatic-hydrothermal magnetite and indicate that the variable degrees of alteration in the Mantoverde district (Cornejo et al. 2000; Rieger et al. 2010) did not significantly alter the primary $\delta^{56}Fe$ signatures of magnetite (Fig. 4). Low-temperature growth of magnetite from a hydrothermal fluid, extensive hydrothermal alteration of magnetite, such as partial or total dissolution, transport, and reprecipitation (Weis 2013; Troll et al. 2019), or Fe ion exchange between a mineral and magnetite above the closure temperature (Frost et al. 2007) result in $\delta^{56}Fe < 0.0$‰. This is clearly seen in the data for the Dannemora iron-skarn in Sweden reported by Lager (2001) who documented multiple episodes of low-temperature dissolution, mobilization, and reprecipitation of magnetite that modified the original $\delta^{56}Fe$ values of magnetite. Similarly, Valley et al. (2011) reported that magnetite-rich ore bodies within the Lyon Mountain Granite, near Mineville, New York, were subjected to extensive sodic alteration, which resulted in albitization and complete dissolution and remobilization of originally magmatic/magmatic-hydrothermal magnetite that significantly altered the $\delta^{56}Fe$ values of magnetite. The new $\delta^{56}Fe$ data for magnetite reported here unequivocally indicate silicate magma as the source Fe.

The $\delta^{56}Fe$ values reported here for late-stage hematite overlap the values reported for magnetite and fall within the range reported for magmatic and magmatic-hydrothermal magnetite. Experimental data indicate negligible Fe isotope

Fig. 3 BSE images (**a**–**c**) of magnetite and FE-SEM EDX maps (**d**–**f**) of Si concentrations in the same magnetite grains from sample depths 298 and 305 m. **a, d** Concentric and oscillatory zoning of trace element-rich and trace element-poor growth bands. **b, c, e, f** Concentric zoning with trace element-rich cores and trace element-poor rims. Bright spots within magnetite in (**d**)–(**f**) are aluminosilicate inclusions
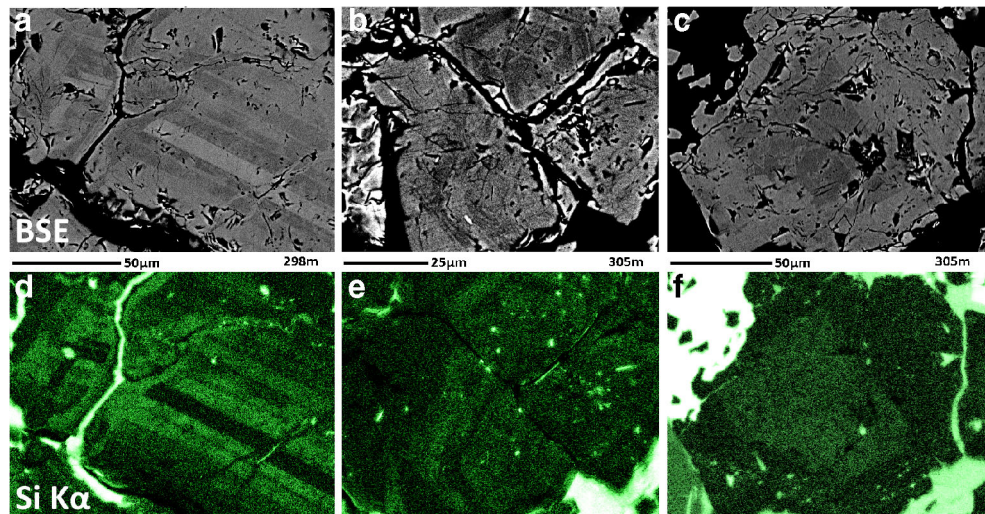
fractionation between oxidized Fe^{3+}-bearing aqueous fluid and hematite at 200 °C (Saunier et al. 2011). Considering that reduced isotopic partition function ratios (β-factors) for magnetite and hematite are similar (Polyakov et al. 2007; Blanchard et al. 2009), isotopic fractionation among these minerals and other phases will be similar. Thus, the hematite δ^{56}Fe data are consistent with a silicate magma source for Fe

and precipitation of hematite from oxidized magmatic-hydrothermal fluid.

Oxygen isotopes The δ^{18}O values (Fig. 5) are consistent with δ^{18}O values reported by Benavides et al. (2007) that range from 1.4 to 3.1‰ for magnetite from the sulfide-bearing orebodies at Mantoverde and from 2.2 to 4.1‰ for magnetite
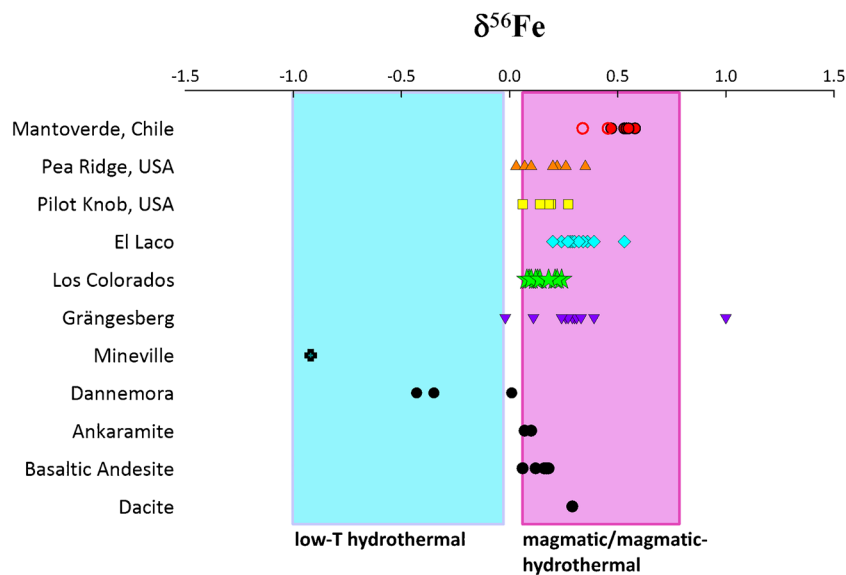

Fig. 4 Iron isotope values (δ^{56}Fe) for primary magnetite (filled red circles) and hematite (open red circles) from Mantoverde along with δ^{56}Fe values for magnetite from several iron oxide—apatite deposits and volcanic reference materials. Symbols correspond to the ore deposit or igneous reference material in the same row on the left side of the plot. The pink box represents the published global range of δ^{56}Fe values (~ 0.0–0.86‰) for igneous and magmatic-hydrothermal magnetite. The blue box represents the published global range of δ^{56}Fe values (− 1.0–

0.0‰) for magnetite that formed from low-temperature hydrothermal processes. Solid symbols for Mantoverde represent magnetite samples, and open symbols represent hematite samples. The data for other systems and igneous reference materials are from ranges from Anbar (2004), Schüßler (2008), Weis (2013), Bilenker et al. (2016), and Childress et al. (2016). The complete Fe isotope data set is provided in Table 4 (ESM)
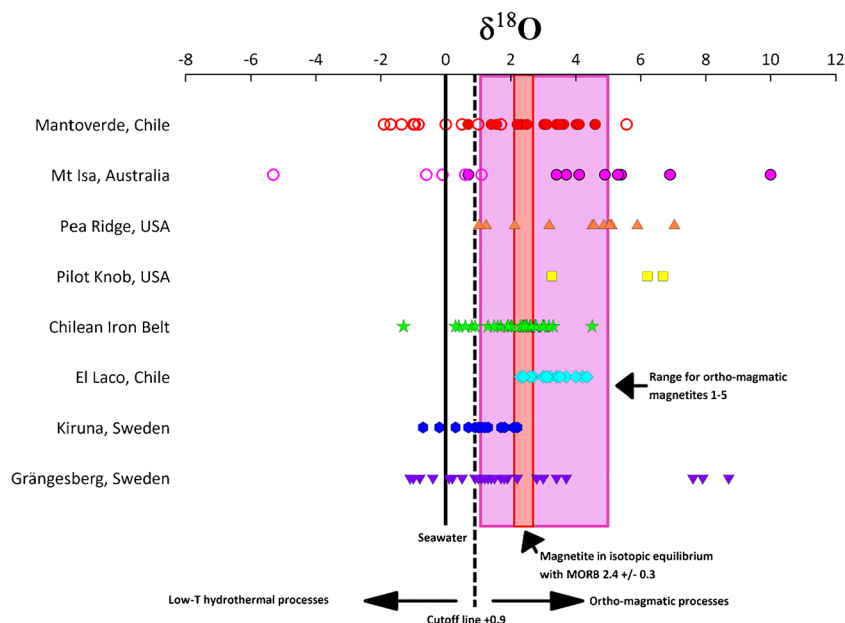
Fig. 5 Oxygen isotope values ($\delta^{18}O$) for primary magnetite and hematite from Mantoverde along with $\delta^{18}O$ values for magnetite from the eastern Mt Isa Block (Australia) and several IOCG deposits including deposits from the Chilean Iron Belt. The pink box represents the global range for $\delta^{18}O$ values (~1–5‰) for magmatic-hydrothermal magnetite. The orange box represents the $\delta^{18}O$ range (2.4 ± 0.3‰) for magnetite in isotopic equilibrium with MORB. The vertical dashed line at ~ $\delta^{18}O$ = 1.0‰ represents the divide between magmatic-hydrothermal magnetite and magnetite crystallized from non-magmatic low-temperature hydrothermal fluids. The solid symbols represent $\delta^{18}O$ values for magnetite samples, and the open symbols represent $\delta^{18}O$ values for hematite samples. Data are from Marshal and Oliver (2006), Nyström et al. (2008), Weis (2013), Jonnson et al. (2014), Bilenker et al. (2016), Childress et al. (2016), and Bilenker et al. (2017). Full list of data are reported in Table 4 (ESM)

from spatially associated magnetite-apatite ± pyrite bodies located along the eastern branch of the Atacama Fault Zone. The new $\delta^{18}O$ values reported here for magnetite are plotted in Fig. 5. Globally, $\delta^{18}O$ values for magnetite in the range of ~ 1 to 5.0‰ indicate crystallization of magnetite from silicate magma or magmatic-hydrothermal fluid, whereas low-temperature growth of magnetite from a hydrothermal fluid, extensive hydrothermal alteration of magnetite, such as partial or total dissolution, transport, and reprecipitation, result in a $\delta^{18}O$ value < 0.9‰ (Taylor 1967; Jonsson et al. 2013; Troll et al. 2019). The $\delta^{18}O$ data for magnetite from Mantoverde indicate that oxygen was derived from a silicate magma source. The magnetite sample that yielded a $\delta^{18}O$ value of 0.69‰ likely reflects alteration, similar to results reported for magnetite from the Kiruna and Grängesberg districts, Sweden (Jonsson et al. 2013; Troll et al. 2019).

The $\delta^{18}O$ values for hematite reported here are, except for one sample that yielded a $\delta^{18}O$ value of + 5.57‰, lighter than values reported for magnetite. We used the average $\delta^{18}O$ values for magnetite and hematite reported here with published values for $\delta^{18}O$ of quartz and calcite from Mantoverde (Rieger et al. 2012) and quartz-fluid and calcite-fluid fractionation factors from Zheng (1991) and

Cole et al. (2004), respectively, to calculate theoretical $\delta^{18}O$ values for hydrothermal fluids that would have been in equilibrium with iron oxide stage magnetite and late-stage hematite. These model results, shown in Fig. 6, indicate that the $\delta^{18}O$ values for magnetite reported here are consistent with predicted $\delta^{18}O$ values. However, the $\delta^{18}O$ values for late-stage hematite reported here indicate a heavier fluid (i.e., greater magmatic component) than predicted by using published $\delta^{18}O$ values of late-stage calcite and calcite-fluid fractionation factors. The model results for $\delta^{18}O$ of late-stage hematite agree with $\delta^{56}Fe$ of late-stage hematite and are consistent with hematite precipitation from oxidized magmatic-hydrothermal fluid.

Trace element compositions of magnetite and hematite

The concentrations of [Al + Mn] vs. [Ti + V] for magnetite and hematite from Mantoverde are plotted on the magnetite discriminant diagram in Fig. 7 along with data for magnetite from the Los Colorados IOA deposit from Knipping et al. (2015a, b). This diagram was originally developed by Dupuis and Beaudoin (2011) and

Fig. 6 The ranges of δ¹⁸O values for model (theoretical) hydrothermal fluids in equilibrium with ore-stage magnetite and late-stage hematite at Mantoverde. The fractionations were calculated by using average δ¹⁸O values for ore-stage quartz and late-stage calcite from Rieger et al. (2012)
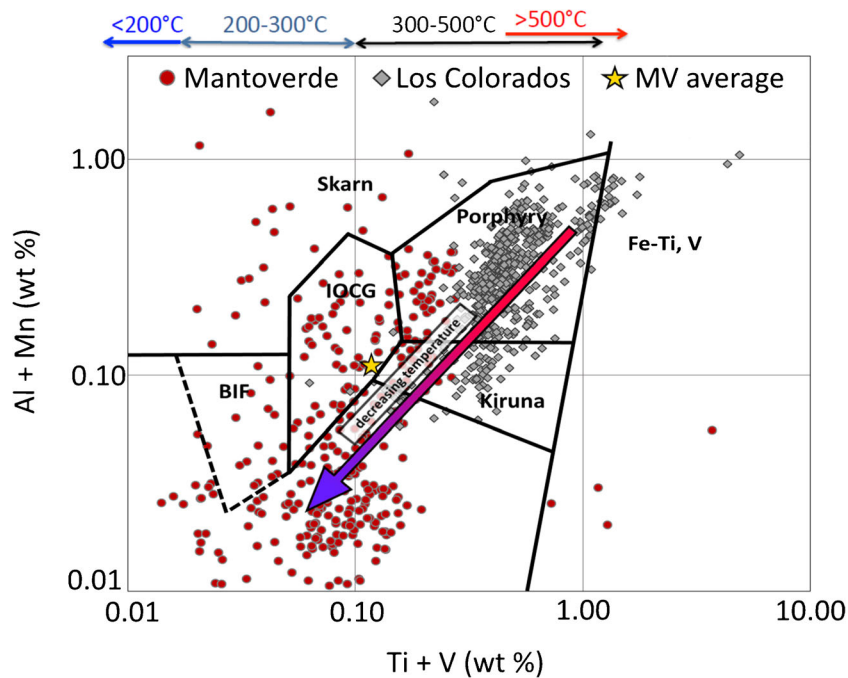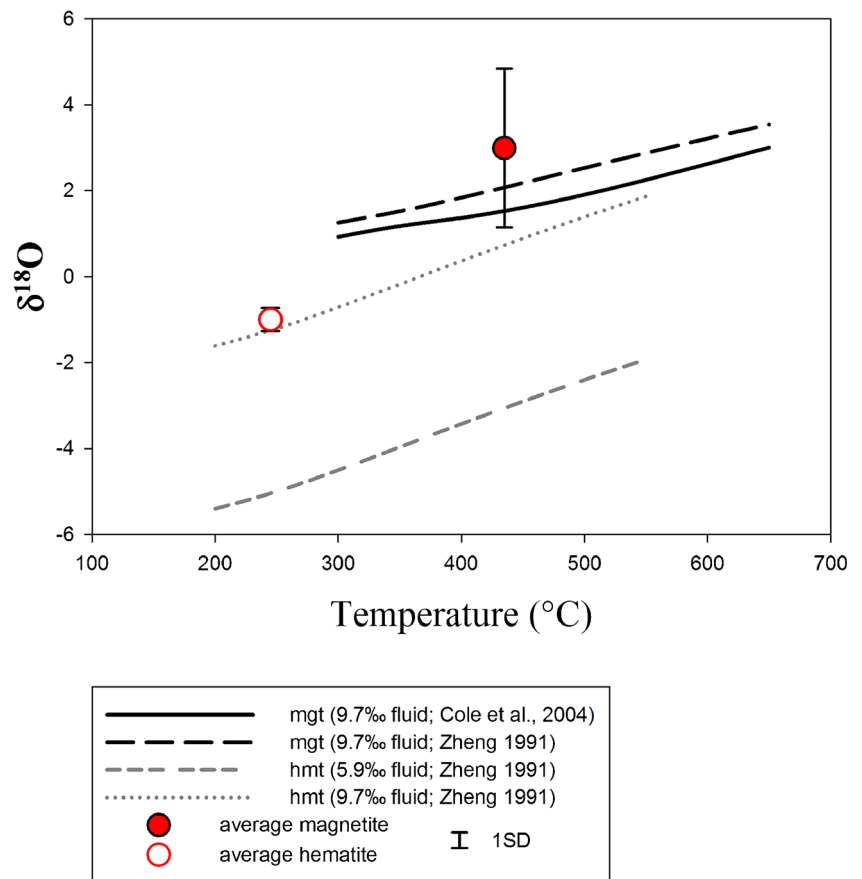

Fig. 7 The concentrations of [Al + Mn] vs. [Ti + V] for magnetite from the Mantoverde IOCG deposit are plotted on the magnetite trace element discrimination diagram from Nadoll et al. (2014), along with [Al + Mn] vs. [Ti + V] for magnetite from the Los Colorados Kiruna-type IOA deposit in the Chilean Iron Belt. The data from Los Colorados are from Knipping et al. (2015a, b). The temperatures on the top abscissa are from Nadoll et al. (2014). The color-graded arrow indicates the expected trend for the trace element chemistry of magnetite that grows from a cooling magmatic-hydrothermal fluid. Data are located in Tables 2, 5, and 6 (ESM)

modified by Nadoll et al. (2014) to discriminate primary magnetite among the c=10?>Kiruna-type IOA, porphyry Cu–Mo(–Au), Fe–Ti–V, and banded iron formations. The average [Ti + V] and [Al + Mn] concentrations for all magnetite analyses from Mantoverde plot in the IOCG field on Fig. 7. However, [Ti + V] and [Al + Mn] concentrations within and among magnetite grains spread across all fields. There is no apparent correlation between trace element concentrations of magnetite and sample depth. The trace element data for magnetite are consistent with data reported by Rieger et al. (2010) for samples from Mantoverde Norte and Sur. The average [Al + Mn] and [Ti + V] values for late-stage hematite from Mantoverde plot in the Kiruna field, and the trace element compositions of individual hematite grains plot across the Kiruna, IOCG, porphyry and Fe-Ti-V fields; the hematite data are not included in Fig. 7.

In spite of the scatter, the values of [Al + Mn] and [Ti + V] for magnetite from Mantoverde are, generally, positively correlated with each other and can be used to assess temperatures of mineralization by comparison with data from Nadoll et al. (2014). Those authors used homogenization temperatures of fluid inclusions hosted in minerals coeval with magnetite from Fe–Ti–V, porphyry, Kiruna, IOCG, skarn, and banded iron formation ore deposits to correlate the abundances of [Al + Mn] and [Ti + V] in magnetite with temperatures of mineralization. Nadoll et al. (2014) reported that magnetite with [Al + Mn] of 0.001–0.1 wt.% and [Ti + V] of 0.0008–0.01 wt.% crystallized from hydrothermal fluid at < 200 °C, [Al + Mn] of 0.01 - 0.2 wt. % and [Ti + V] of 0.001 - 0.1 wt. % crystallized from hydrothermal fluid at 200 - 300 °C, [Al + Mn] of 0.1 - 3 wt. % and [Ti + V] of 0.03 - 1 wt. % crystallized from hydrothermal fluid at 300 - 500 °C, and [Al + Mn] >0.1 wt. % and [Ti + V] >0.3 wt. % crystallized from hydrothermal fluid at >500 °C; see top x-axis of Fig. 7. These temperature ranges indicate that the trace element chemistry of magnetite systematically changes from high temperature to low temperature; i.e., from igneous Fe-Ti-V deposits to banded iron formations. These results based on Al, Mn, Ti and V concentrations are consistent with other studies and the expectation that the magnetite lattice is more accommodating for trace element incorporation at high temperature. For example, Neumann et al. (2017) studied magnetite from the Angara-Ilim IOCG deposit in Siberia and reported that the concentrations of Ca, Al, Mg, and Si in hydrothermal magnetite systematically decreased as magnetite crystallized from a cooling ore fluid. The concentrations of Ca vs. Al (Fig. 8a), Ca vs. Si (Fig. 8c), and Si vs. Al (Fig. 8e)

in magnetite and hematite from Mantoverde are also consistent with cooling trend.

The cooling trend is supported by microthermometry data for magnetite-bearing fluid inclusions in coeval iron oxide stage quartz from Mantoverde that indicate mineralization occurred over a temperature range from 530 to 278 °C (Rieger et al. 2012). Those authors also reported homogenization temperatures for fluid inclusions in late-stage calcite that indicate late-stage hematite crystallization occurred between 462 and 221 °C. These temperature ranges, when combined with the trace element concentrations in magnetite and hematite, are consistent with the cooling trends shown schematically in Figs. 7 and 8.

A magmatic-hydrothermal model genesis for Mantoverde

The δ^{56}Fe and δ^{18}O data for magnetite and hematite from Mantoverde (Fig. 9) are consistent with a silicate magma source for Fe and O, the most abundant elements in the mineralized system. These data complement published data for isotopes of C, O, S, Sr, Pb, Ar, Kr, Xe, and halogen ratios for samples from Mantoverde that consistently indicate silicate magma as the source of the ore fluid for the Mantoverde district (Benavides et al. 2007, 2008; Rieger et al. 2010, 2012; Marschik and Kendrick 2015). Some data, for example δ^{18}O values in late-stage hematite, do reveal the presence of a non-magmatic fluid, plausibly a basinal brine, but the sum of the isotopic data indicate that such a fluid was volumetrically minor and present only during the waning stages of mineralization. The trace element chemistry of magnetite and hematite and published fluid inclusion homogenization temperatures (Rieger et al. 2012) are consistent with mineralization from a cooling magmatic-hydrothermal ore fluid that formed the magnetite-rich iron oxide stage at temperatures between 530 and 278 °C followed by intermediate to shallow level Sulfide Stage mineralization over the range 325 to 221 °C, and late-state hematite and calcite stage over the range 462 and 221 °C (Benavides et al. 2007; Rieger et al. 2012).

It has been hypothesized that IOCG deposits represent the shallow part of systems that transition with depth to IOA mineralization (Sillitoe 2003). A new genetic model linking IOCG deposits and IOA deposits was proposed by Knipping et al. (2015a) based on the major, minor and trace element concentrations and Fe and O stable isotope abundances of magnetite from the Los Colorados IOA deposit in the Chilean Iron Belt that reveal magnetite
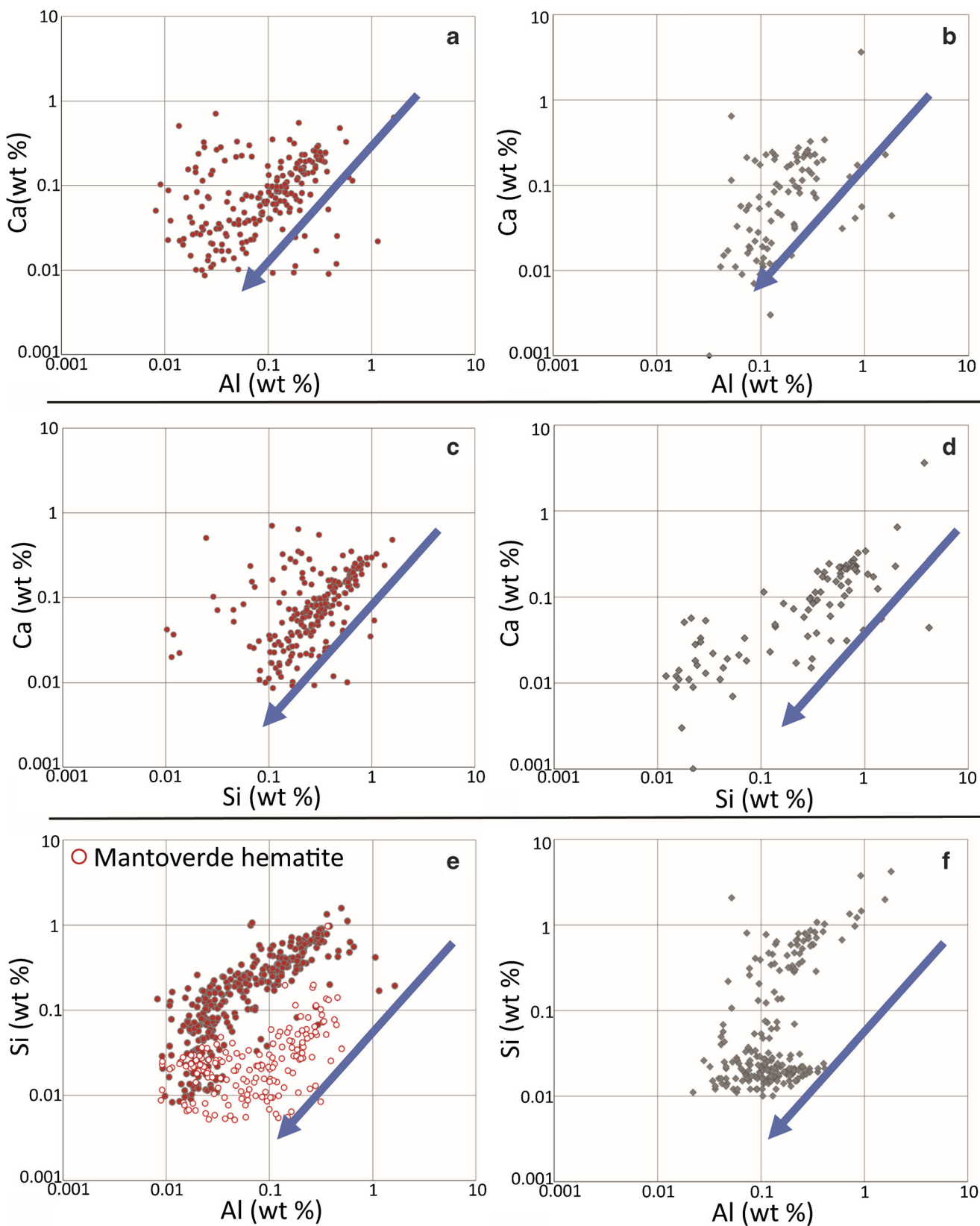
Fig. 8 The trace element compositions of magnetite from the Mantoverde IOCG deposit and the Los Colorados IOA deposit are plotted as weight percents of Ca vs. Al (**a**, **b**), Ca vs. Si (**c**, **d**), and Si vs. Al (**e**, **f**). The symbols are the same as those used in Fig. 7. Only data from drill core LC-04 that intersects the main massive magnetite ore body at Los Colorados are plotted (Knipping et al. 2015b). Hematite is only plotted in (**e**) owing to lack of detectable Ca concentrations. The concentrations of Mg vs. Si, not included here, show very similar correlations. The blue arrows denote the trend expected if magnetite and hematite grow from a cooling magmatic-hydrothermal fluid
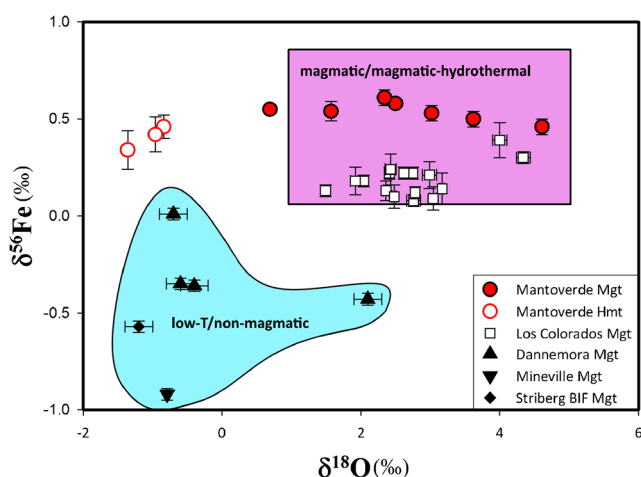
Fig. 9 Oxygen (δ^{18}O) and iron (δ^{56}Fe) isotope values determined for the same primary magnetite and hematite samples from Mantoverde are plotted. The pink box represents the global range of δ^{18}O and iron δ^{56}Fe values reported for igneous and magmatic-hydrothermal magnetite (Weis 2013; Bilenker et al. 2016). The error bars plotted for both δ^{18}O and δ^{56}Fe values are 2σ, and some δ^{18}O error bars are smaller than the symbols. Data in Tables 3 and 4 (ESM)

contains both an igneous and a magmatic-hydrothermal chemical signature. Those authors report that, systematically, magnetite cores are chemically equivalent to magnetite grown from a silicate melt, and magnetite rims are chemically equivalent to magnetite grown from cooling magmatic-hydrothermal fluid. Their genetic model invokes crystallization of magnetite nanolites (cores) from a silicate melt that subsequently reached volatile saturation whereupon magnetite crystal surfaces served as nucleation sites for an exsolving magmatic-hydrothermal volatile phase (Hurwitz and Navon 1994). Initial growth of magnetite in equilibrium with silicate melt is indicated by the enrichment of trace elements such as Ti, V, Al, Mn, Si, Ca in magnetite cores, which also contain polycrystalline silicate melt inclusions that rehomogenize at >850 °C (Knipping et al. 2015b). Regional extension allowed the magma to ascend along pre-existing faults and, during decompression, resulted in the formation of a magnetite-fluid suspension that ascended from the source magma. Growth of magnetite rims from an Fe-rich magmatic-hydrothermal fluid is indicated by the trace element chemistry of magnetite and also the presence of halite-bearing fluid inclusions in the rims of magnetite. The concentrations of trace elements in magnetite systematically decrease from core to rim and across the rim, consistent with magnetite growth from a cooling magmatic-hydrothermal fluid (Nadoll et al. 2014). A magnetite-fluid suspension is buoyant as long as the proportion of magnetite is < 37

vol.% of the suspension. The model was tested experimentally by Knipping et al. (2019) who demonstrated that magnetite microlites attach to Cl-bearing H_2O bubbles and form a magnetite-fluid suspension that ascends quite efficiently through andesitic melt.

Knipping et al. (2015a) proposed that regional changes in tectonic stress can rapidly destabilize a magma body and cause the magnetite-fluid suspension at the top of the magma chamber to ascend from its source magma along pre-existing faults. During ascent, original igneous magnetite crystals will source Fe and O from the fluid and rims will grow around the igneous magnetite. The trace element contents of the magnetite rims will reflect growth from a magmatic-hydrothermal fluid as the fluid cools. These magnetite grains will eventually become too dense for the fluid to continue to transport, and they will drop out of the fluid suspension when they reach a level of neutral buoyancy, forming the structurally controlled massive magnetite orebodies such as those at Los Colorados. Depending on the permeability-porosity of the host rocks adjacent to the fault, the hydrothermal fluid may migrate into the host rocks and form disseminated orebodies, commonly observed in IOA deposits. Data from natural systems (Williams-Jones and Heinrich 2005) and experimental studies (Chou and Eugster 1977; Wood and Samson 1998; Simon et al. 2004; Hurtig and Williams-Jones 2014; Williams-Jones and Migdisov 2014) demonstrate that the fluid will be enriched in S and metals such as Fe, Cu, and Au as it cools to temperatures < 500 °C. Thus, the hydrothermal fluid is capable of precipitating iron oxides and metal sulfides during decompression and cooling above and proximal to magnetite-rich IOA orebodies.

Three chemical groups of pyrite were found to exist in the Mantoverde IOCG deposit, containing Co/Ni ratios of < 1, 1–20, and > 90, partially overlapping Co/Ni ratios from Los Colorados (Reich et al. 2016; Johansson et al. 2017). These ratios grade high (i.e., > 90) to low (i.e., < 1) from the deeper sections of the deposit to the shallow sections, indicative of a cooling and evolving fluid. Iron oxide-copper-gold orebodies within the Mantoverde district are also spatially and temporally associated with magnetite-apatite ± pyrite mineralization (Benavides et al. 2008; Rieger et al. 2010), and it seems geologically plausible that the formation of the Mantoverde system is consistent with the combined igneous/magmatic-hydrothermal model proposed by Knipping et al. (2015a) that predicts a cooling trend for the trace element chemistry of magnetite in the sulfur-poor IOA orebodies and magnetite in the sulfur-enriched IOCG orebodies. This is exactly what is observed in the trace element chemistry for magnetite from the Mantoverde IOCG deposit.

In Figs. 7 and 8, the Al, Mn, Ti, V, Si, and Ca concentrations of magnetite from Los Colorados (Knipping et al. 2015a, b) are plotted with data from Mantoverde in order to compare the cooling trend reported by those authors with that discussed above for Mantoverde. Bilenker et al. (2016) reported temperatures for magnetite-actinolite pairs determined by O sotope thermometry and Fe # data for actinolite coeval with massive magnetite from the same samples studied by Knipping et al. (2015a, b) that indicate mineralization occurred over the temperature range ~ 600 to 810 °C. Figure 7 reveals a remarkable continuum and predicts the presence of magnetite-rich mineralization at depth in the Mantoverde system, which is corroborated by geophysical data (Mantos Copper, written communication, 4 July 2017). These two ore deposits are not genetically related, but this is consistent with the combined igneous/magmatic-hydrothermal flotation model proposed by Knipping et al. (2015a, b) that explains the geologic and geochemical observations for each deposit.

Conclusions

Fe and O isotope data for iron oxide stage magnetite and Late Stage hematite from the Mantoverde IOCG deposit, combined with published data for isotopic compositions of C, O, S, Sr, Pb, Ar, Kr, and Xe for hypogene samples from the Mantoverde district, support a magmatic-hydrothermal genesis. Magnetite cores are enriched in Ti, V, Mn, Si, Al, Mg, and Ca relative to surrounding rims, indicating that magnetite grew from an initially hotter and gradually cooling source-fluid. Oxygen isotope $\delta^{18}O$ values vary among individual magnetite and hematite samples due to variable degrees of hydrothermal alteration, supported by widely varying Al, Ca, Mn, Ti, and V concentrations in magnetite and hematite, while Fe isotope $\delta^{56}Fe$ values remain relatively unaffected by hydrothermal alteration and, when coupled with O isotopes, are a robust tool to differentiate between magmatic and meteoric fluid sources.

References

Anbar AD (2004) Iron stable isotopes: beyond biosignatures. Earth Planet Sci Lett 217:223–236

Barra F, Reich M, Rojas P, Selby D, Simon AC, Salazar E, Palma G (2017) Unraveling the origin of the Andean IOCG Clan: a Re-Os isotope approach. Ore Geol Rev 81:62–78

Barton MD (2014) Iron oxide (–Cu–Au–REE–P–Ag–U–Co) systems. In: Scott SD (ed) Geochemistry of mineral deposits. Treatise on Geochemistry, vol 13, 2nd edn. Elsevier, Amsterdam, pp 515–541

Barton MD, Johnson DA (1996) Evaporitic-source model for igneous-related Fe oxide-(REE-Cu-Au-U) mineralization. Geology 26:259–262

Benavides J, Kyser TK, Clark AH, Oates CJ, Zamora R, Tarnovschi R, Castillo B (2007) The Mantoverde iron oxide-copper-gold district, III Región, Chile: the role of regionally derived, non-magmatic fluids in chalcopyrite mineralization. Econ Geol 102:415–440

Benavides J, Kyser TK, Clark AH, Stanley C, Oates CJ (2008) Exploration guidelines for copper-rich iron oxide–copper–gold deposits in the Mantoverde area, northern Chile: the integration of host-rock molar element ratios and oxygen isotope compositions. Geochem Explor Environ Anal 8:343–367

Bilenker LD, Simon AC, Reich M, Lundstrom CC, Gajos N, Bindeman I, Barra R, Munizaga R (2016) Fe-O stable isotope pairs elucidate a high-temperature origin of Chilean iron oxide-apatite deposits. Geochim Cosmochim Acta 177:94–104

Bilenker LD, VanTongeren JA, Lundstrom CC, Simon AC (2017) Iron isotopic evolution during fractional crystallization of the uppermost Bushveld Complex layered mafic intrusion. Geochemistry Geophysics Geosystems 18. https://doi.org/10.1002/2016GC006660.

Blanchard M, Poitrasson F, Méheut M, Lazzeri M, Mauri F, Balan E (2009) Iron isotope fractionation between pyrite (FeS₂), hematite (Fe₂O₃) and siderite (FeCO₃): a first-principles density functional theory study. Geochim Cosmochim Acta 73:6565–6578

Childress TM, Simon AC, Day WC, Lundstrom CC, Bindeman IN (2016) Iron and oxygen isotope signatures of the Pea Ridge and Pilot Knob magnetite-apatite deposits, Southeast Missouri, USA. Econ Geol 111:2033–2044

Chou IM, Eugster HP (1977) Solubility of magnetite in supercritical chloride solutions. Am J Sci 277:1296–1314

Cole DR, Horita J, Polyakov VB, Valley JW, Spicuzza MJ, Coffey DW (2004) An experimental and theoretical determination of oxygen isotope fractionation in the system magnetite-H₂O from 300 to 800 °C. Geochim Cosmochim Acta 68:3569–3585

Cornejo P, Matthews S, Orrego M, Robles W (2000) Etapas de mineralización asociadas a alteración potásica en un sistema Fe-Cu-Au: Yacimiento Mantoverde, III Región de Atacama, Chile: IX Congreso Geológico Chileno, Puerto Varas, Actas, pp 97–101.

Craddock PR, Dauphas N (2011) Iron isotopic compositions of geological reference materials and chondrites. Geostand Geoanal Res 35: 101–123

Dare SAS, Barnes S-J, Beaudoin G (2014) Did the massive magnetite "lava flows" of El Laco (Chile) form by magmatic or hydrothermal processes? New constraints from magnetite composition by LA-ICP-M. Mineral Deposita 50:607–617

Dupuis C, Beaudoin G (2011) Discriminant diagrams for iron oxide trace element fingerprinting of mineral deposit types. Mineral Deposita 46:319–335

Fisher LA, Kendrick MA (2008) Metamorphic fluid origins in the Osborne Fe oxide-Cu-Au deposit, Australia: evidence from noble gases and halogens. Mineral Deposits 43:483–497

Frost CD, von Blanckenburg F, Schoenberg R, Frost BR, Swapp SM (2007) Preservation of Fe isotope heterogeneities during diagenesis and metamorphism of banded iron formation. Contrib Mineral Petrol 153:211–235

Groves DI, Bierlein FP, Meinert LD, Hitzman MW (2010) Iron oxide copper-gold (IOCG) deposits through earth history: implications for origin, lithospheric setting, and distinction from other epigenetic iron oxide deposits. Econ Geol 105:641–654

Heimann A, Beard BL, Johnson CM (2008) The role of volatile exsolution and subsolidus fluid/rock interactions in producing high ^{56}Fe/^{54}Fe ratios in siliceous igneous rocks. Geochim Cosmochim Acta 72:4379–4396

Hitzman MW, Oreskes N, Einaudi MT (1992) Geological characteristics and tectonic setting of Proterozoic iron oxide (Cu-U-Au-REE) deposits. Precambrian Res 58:241–287

Huang F, Zhang Z, Lundstrom CC, Zhi X (2011) Iron and magnesium isotopic compositions of peridotite xenoliths from eastern China. Geochim Cosmochim Acta 75:3318–3334

Hurtig NC, Williams-Jones AE (2014) An experimental study of the transport of gold through hydration of AuCl in aqueous vapour and vapour-like fluids. Geochim Cosmochim Acta 127:305–325

Hurwitz S, Navon O (1994) Bubble nucleation in rhyolitic melts: experiments at high pressure, temperature, and water content, Earth Planet. Sci Lett 122:267–280

Johansson C, Barra F, Reich M, Deditius AP, Simon AC, Rojas P (2017) The Co-Ni signature of sulfide minerals from the Mantoverde IOCG deposit, northern Chile. Goldschmidt Abstracts, 1871

Jonsson E, Valentin RT, Högdahl K, Harri C, Weis F, Nilsson KP, Skelton A (2013) Magmatic origin of giant 'Kiruna-type' apatite-iron-oxide ores in central Sweden. Sci Rep 3. https://doi.org/10.1038/srep01644

Knipping JL, Bilenker LD, Simon AC, Reich M, Barra F, Deditius AP, Lundstrom C, Bindeman I, Munizaga R (2015a) Giant Kiruna-type deposits form by efficient flotation of magmatic magnetite suspensions. Geology 43:491–594

Knipping JL, Bilenker LD, Simon AC, Reich M, Barra F, Deditius AP, Wälle M, Heinrich CA, Holtz F, Munizaga R (2015b) Trace elements in magnetite from massive iron oxide-apatite deposits indicate a combined formation by igneous and magmatic hydrothermal processes. Geochim Cosmochim Acta 171:15–38

Knipping J, Webster JD, Simon AC, Holtz F (2019) Accumulation of magnetite by flotation on bubbles during decompression of silicate magma. Sci Rep 9:3852

Lager I (2001) The geology of the Palaeoproterozoic limestone-hosted Dannemora iron deposit. The Geological Survey of Sweden, Sweden 54 p

Lara L, Godoy E (1998) Hoja quebrada salitrosa, III Región de Atacama: Santiago, Chile. Servicio Nacional de Geología y Minería, Mapas Geológicos 4, escala 1:100,000

Marschik R, Kendrick MA (2015) Noble gas and halogen constraints on fluid sources in iron oxide-copper-gold mineralization: Mantoverde and La Candelaria, Northern Chile. Mineral Deposita 50:357–371

Marshal LJ, Oliver NHS (2006) Monitoring fluid chemistry in IOCG-related metasomatic processes, eastern Mt Isa Block, Australia. Geofluids 6:45–66

Millet MA, Baker JA, Payne CE (2012) Ultra-precise stable Fe isotope measurements by high resolution multiple-collector inductively coupled plasma mass spectrometry with a 57Fe-58Fe double spike. Chem Geol 304:18–25

Mpodozis C, Ramos V (1990) The Andes of Chile and Argentina: circum-Pacific council for energy and mineral resources. Earth Sci Ser 11:59–90

Mumin AH, Somarin AK, Jones B, Corriveau L, Ootes L, Camier J (2010) The IOCG-porphyry-epithermal continuum in the Great Bear Magmatic Zone, Northwest Territories, Canada. In: Corriveau L and Mumin AH (eds) Exploring for iron oxide copper-gold deposits: Canada and Global analogues. Geological Association of Canada, Short Course Number 20, pp 59–78

Nadoll P, Angerer T, Mauk JL, French D, Walshe J (2014) The chemistry of hydrothermal magnetite: a review. Ore Geol Rev 61:1–32

Naslund HR, Henriquez F, Nyström JO, Vivallo W, Dobbs FM (2002) Magmatic iron ores and associated mineralisation: examples from the Chilean high Andes and coastal Cordillera. In: Porter TM (ed) Hydrothermal iron oxide copper–gold: a global perspective, 2nd edn. PGC Publishing, Adelaide, pp 207–226

Neumann E-R, Svensen HH, Polozov AG, Hammer Ø (2017) Formation of Si-Al-Mg-Ca-rich zoned magnetite in an end-Permian phreatomagmatic pipe in the Tunguska Basin, East Siberia. Mineral Deposita 52:1205–1222

Nyström JO, Henríquez F (1994) Magmatic features of iron ores of the Kiruna-type in Chile and Sweden: ore textures and magnetite geochemistry. Econ Geol 89:820–839

Nyström JO, Billström K, Henríquez F, Fallick AE, Naslund HR (2008) Oxygen isotope composition of magnetite in iron ores of the Kiruna type in Chile and Sweden: GFF [Geologiska Föreningen]. 130:177–188

Pollard PJ (2006) An intrusion-related origin for Cu-Au mineralization in iron oxide-copper-gold (IOCG) provinces. Mineral Deposita 41:179–187

Polyakov VB, Clayton RN, Horita J, Mineev SD (2007) Equilibrium iron isotope fractionation factors of minerals: Reevaluation from the data of nuclear inelastic resonant X-ray scattering and Mössbauer spectroscopy. Geochim Cosmochim Acta 71:3833–3846

Porter TM (ed) (2000) Hydrothermal iron oxide copper-gold and related deposits: a global perspective. Australian mineral Foundation, Adelaide 349 p

Reich M, Simon AC, Deditius A, Barra F, Chryssoulis S, Lagas G, Tardani D, Knipping J, Bilenker L, Sanchez-Alfaro P, Roberts MP, Munizaga R (2016) Trace element signature of pyrite from the Los Colorados iron oxide-apatite (IOA) deposit, Chile: a missing link between Andean IOA and IOCG systems? Econ Geol 111:743–761

Richards JP, Mumin AH (2013a) Lithospheric fertilization and mineralization by arc magmas: Genetic links and secular differences between porphyry copper±molybdenum±gold and magmatic-hydrothermal iron oxide copper-gold deposits. In: Colpron M, Bissig T, Rusk BG, Thompson JFH (eds) Tectonics, metallogeny, and discovery: the North American Cordillera and Similar Accretionary Settings, vol 17. Society of Economic Geologists, Special Publication, pp 277–299

Richards JP, Mumin AH (2013b) Magmatic-hydrothermal processes within an evolving Earth: iron oxide-copper-gold and porphyry Cu ± Mo ± Au deposits. Geology. https://doi.org/10.1130/G34275.1

Rieger AA, Marschik R, Díaz M, Hölzl S, Chiaradia M, Akker B, Spangenberg JE (2010) The hypogene IOCG mineralization in the Mantoverde district, northern Chile. Econ Geol 105:1271–1299

Rieger AA, Marschik R, Díaz M (2012) The evolution of the hydrothermal IOCG system in the Mantoverde district, northern Chile: new evidence from microthermometry and stable isotope geochemistry. Mineral Deposits 47:359–369

Roberts DE, Hudson GRT (1983) The Olympic Dam copper-uranium-gold-silver deposit, Roxby Downs, South Australia. Econ Geol 78:799–822

Saunier G, Pokrovski GS, Poitrasson F (2011) First experimental determination of iron isotope fractionation between hematite and aqueous solution at hydrothermal conditions. Geochim Cosmochim Acta 75:6629–6645

Schüßler J (2008) Controls on stable iron isotope variations in magmatic systems—significance of mineral-melt isotopic fractionation in experiments and nature. Unpublished Ph.D. thesis, Faculty of Natural Science, Gottfried Wilhelm Leibniz Universität, Hannover, Germany, 165 p

Sillitoe RM (2003) Iron oxide-copper-gold deposits: An Andean view. Mineral Deposita 38:787–812

Sillitoe RM, Burrows DR (2002) New field evidence bearing on the origin of the El Laco magnetite deposit, northern Chile. Econ Geol 97:1101–1109

Simon AC, Pettke T, Candela PA, Piccoli PM, Heinrich CA (2004) Magnetite solubility and iron transport in magmatic-hydrothermal environments. Geochim Cosmochim Acta 68:4905–4914

Simon AC, Knipping J, Reich M, Barra F, Deditius AP, Bilenker L, Childress T (2018) Kiruna-type iron oxide-apatite (IOA) and iron oxide copper-gold (IOCG) deposits form by a combination of igneous and magmatic-hydrothermal processes: evidence from the Chilean Iron Belt. Soc Econ Geol Special Publication No 21:89–114

Taylor HP (1967) Oxygen isotope studies of hydrothermal mineral deposits. In: Barnes HL (ed) Geochemistry of hydrothermal ore deposits, 1st edn. Holt, Rinehart and Winston, New York, pp 109–142

Tornos F, Velasco F, Hanchar JM (2016) Iron-rich melts, magmatic magnetite, and superheated hydrothermal systems: the El Laco deposit, Chile. Geology 44(6):427–430

Travisany V, Henriquez F, Nyström JO (1995) Magnetite lava flows in the Pleito-Melon District of the Chilean iron belt. Econ Geol 90:438–444

Troll VR, Weis FA, Jonsson E, Andersson UB, Majidi SA, Högdahl K, Harris C, Millet MA, Chinnasamy SS, Kooijman E, Nilsson KP (2019) Global Fe-O isotope correlation reveals mamatic origin of Kiruna-type apatite-iron-oxide ores. Nature Communications 10(1):1712

Valley PM, Hanchar JM, Whitehouse MJ (2011) New insights on the evolution of the Lyon Mountain Granite and associated Kiruna-type magnetite-apatite deposits: Adirondack Mountains, New York State. Geosphere 7:357–389

Vila T, Lindsay N, and Zamora R (1996) Geology of the Mantoverde copper deposit, northern Chile: a specularite-rich hydrothermal tectonic breccia related to the Atacama fault zone. Soc Econ Geol Special Publication 5:157–170

Weis F (2013) Oxygen and iron isotope systematics of the Grängesberg mining district (GMD), central Sweden. Unpublished Ph.D. Dissertation, Uppsala Universitet, Uppsala, Sweden, 77p

Williams PJ, Barton MD, Johnson DA, Fontboté L, de Haller A, Mark G, Oliver NHS. Marschik R (2005) Iron oxide copper-gold deposits: geology, space-time distribution, and possible modes of origin. Economic Geology 100th Anniversary volume, pp 371–405

Williams-Jones AE, Heinrich CA (2005) Vapor transport of metals and the formation of magmatic-hydrothermal ore deposits. Econ Geol 100:1287–1312

Williams-Jones AE, Migdisov AA (2014) Experimental constraints on the transport and deposition of metals in ore-forming hydrothermal systems. Soc Econ Geol 18:77–96

Wood SA, Samson IM (1998) Solubility of ore minerals and complexation of ore metals in hydrothermal solutions. In: Richards J, Larson P (eds) Techniques in hydrothermal ore deposits. Reviews in Economic Geology 10:33–80.

Zamora R, Castillo B (2001) Mineralizació de Fe-Cu-Au en el distrito Mantoverde, Cordillera de la Costa, III Región de Atacama, Chile: Congreso Internacional de Prospectores y Exploradores, Lima, Conferencias, 2nd edn. Instituto de Ingenieros de Minas del Perú, Lima, Actas, 13p

Zheng Y-F (1991) Calculation of oxygen isotope fractionation in metal oxides. Geochim Cosmochim Acta 55:2299–2307

Affiliations

Tristan M. Childress [1] (iD) · **Adam C. Simon** [1] · **Martin Reich** [2] · **Fernando Barra** [2] · **Mauricio Arce** [3] · **Craig C. Lundstrom** [4] ·
Ilya N. Bindeman [5]

[1]   Department of Earth and Environmental Sciences, University of Michigan, 1100 North University Ave, Ann Arbor, MI 48109-1005, USA

[2]   Department of Geology and Andean Geothermal Center of Excellence (CEGA), Universidad de Chile, Plaza Ercilla 803, Santiago, Chile

[3]   Mantos Copper, Nicolas Tirado 377, Antofagasta, Chile

[4]   Department of Geology, University of Illinois, 605 E. Springfield Ave., Champaign, IL, USA

[5]   Department of Geological Sciences, University of Oregon, 1275 E 13th Ave., Eugene, OR, USA